



# The impact of water on slip system activity in olivine and the formation of bimodal crystallographic preferred orientations

D. Wallis<sup>a,\*</sup>, L.N. Hansen<sup>b</sup>, M. Tasaka<sup>c</sup>, K.M. Kumamoto<sup>d</sup>, A.J. Parsons<sup>b</sup>, G.E. Lloyd<sup>e</sup>, D.L. Kohlstedt<sup>f</sup>, A.J. Wilkinson<sup>g</sup>

<sup>a</sup> Department of Earth Sciences, Utrecht University, Utrecht, 3584 CS, Netherlands

<sup>b</sup> Department of Earth Sciences, University of Oxford, Oxford, OX1 3AN, UK

<sup>c</sup> Department of Geology, Shimane University, Shimane, 6908504, Japan

<sup>d</sup> Department of Geological Sciences, Stanford University, CA, 94305-2210, USA

<sup>e</sup> School of Earth and Environment, University of Leeds, Leeds, LS2 9JT, UK

<sup>f</sup> Department of Earth Science, University of Minnesota-Twin Cities, Minneapolis, MN, 55455, USA

<sup>g</sup> Department of Materials, University of Oxford, Oxford, OX1 3PH, UK

## ARTICLE INFO

### Article history:

Received 6 September 2018

Received in revised form 10 November 2018

Accepted 10 December 2018

Available online xxxx

Editor: J. Brodholt

### Keywords:

olivine

crystallographic preferred orientation

dislocation slip system

HR-EBSD

VPSC

seismic properties

## ABSTRACT

Crystallographic preferred orientations (CPOs) in olivine are widely used to infer the mechanisms, conditions, and kinematics of deformation of mantle rocks. Recent experiments on water-saturated olivine were the first to produce a complex CPO characterised by bimodal orientation distributions of both [100] and [001] axes and inferred to form by combined activity of (001)[100], (100)[001], and (010)[100] slip. This result potentially provides a new microstructural indicator of deformation in the presence of elevated concentrations of intracrystalline hydrous point defects and has implications for the interpretation of seismic anisotropy. Here, we document a previously unexplained natural example of this CPO type in a xenolith from Lesotho and demonstrate that it too may be explained by elevated concentrations of hydrous point defects. We test and confirm the hypothesis that combined (001)[100], (100)[001], and (010)[100] slip were responsible for formation of this CPO by (1) using high-angular resolution electron backscatter diffraction to precisely characterise the dislocation types present in both the experimental and natural samples and (2) employing visco-plastic self-consistent simulations of CPO evolution to assess the ability of these slip systems to generate the observed CPO. Finally, we utilise calculations based on effective-medium theory to predict the anisotropy of seismic wave velocities arising from the CPO of the xenolith. Maxima in S-wave velocities and anisotropy are parallel to both the shear direction and shear plane normal, whereas maxima in P-wave velocities are oblique to both, adding complexity to interpretation of deformation kinematics from seismic anisotropy.

© 2018 The Authors. Published by Elsevier B.V. This is an open access article under the CC BY license (<http://creativecommons.org/licenses/by/4.0/>).

## 1. Introduction

Deformation microstructures, including crystallographic preferred orientations (CPOs), in olivine impact the rheological and other petrophysical properties of mantle rocks and provide key records of deformation events and the processes by which they occur. As such, the impact of water on the rheological properties (e.g., Chopra and Paterson, 1981; Mackwell et al., 1985; Karato et al., 1986; Mei and Kohlstedt, 2000; Tasaka et al., 2015; Tielke et al., 2017), slip system activity, and CPOs (e.g., Zhang et al., 2000; Jung and Karato, 2001; Jung et al., 2006; Skemer et al., 2006;

Demouchy et al., 2012; Tasaka et al., 2016; Bernard and Behr, 2017) of olivine has been an area of intense investigation.

Deformation experiments on olivine aggregates have revealed changes in CPO as a function of water content. Anhydrous olivine typically develops CPOs with a single maximum of [100] axes and distributions of [010] and [001] axes that indicate dominance of the (010)[100] slip system, with subordinate slip on other (*OkI*)[100] systems (A- and D-type CPOs), as demonstrated in Fig. 1 (e.g., Zhang and Karato, 1995; Hansen et al., 2014). In contrast, CPOs developed in aggregates of olivine with elevated concentrations of intracrystalline hydrous point defects are typified by single maxima of [100] and [001] axes in orientations that indicate dominance of *one* of the slip systems (001)[100], (100)[001], or (010)[001] (E-, C-, and B-type CPOs, respectively) (e.g., Katayama et al., 2004; Jung et al., 2006). Such relation-

\* Corresponding author.

E-mail address: [d.wallis@uu.nl](mailto:d.wallis@uu.nl) (D. Wallis).

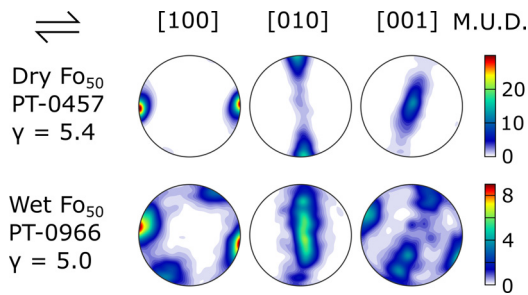


**Fig. 1.** Typical crystallographic preferred orientations developed at shear strain of  $\gamma \approx 5$  during torsion experiments on anhydrous (Hansen et al., 2012) and hydrous (Tasaka et al., 2016)  $\text{Fo}_{50}$  olivine. (For interpretation of the colours in the figure(s), the reader is referred to the web version of this article.)

ships suggest that olivine CPOs potentially provide clues to the conditions of natural deformation events. Experimentally established relationships between the water content and CPO type of olivine are broadly consistent with natural samples for which both have been measured. Olivine in natural samples with low water contents typically exhibits A-type CPO (e.g., Jung et al., 2009; Cao et al., 2015), whereas olivine in natural samples with elevated water contents typically exhibits E-, C-, or B-type CPOs (e.g., Mizukami et al., 2004; Jung et al., 2009, 2013, 2014).

Despite the extent of previous work, experimental deformation of aggregates of water-saturated olivine to high shear strains of  $\gamma > 5$  was only achieved recently (Tasaka et al., 2016). These experiments produced a CPO not seen in previous laboratory-deformed samples (Fig. 1). This CPO exhibits two maxima of both [100] and [001] axes (Tasaka et al., 2016), that is, bimodal distributions in the plane containing the shear direction and shear plane normal. [010] axes form a maximum perpendicular to both the shear direction and the shear plane normal and are somewhat girdled toward the shear plane normal. Based on the CPO, analysis of subgrain boundaries, and previous deformation experiments, Tasaka et al. (2016) inferred that this CPO formed by slip on the (001)[100], (100)[001], and to a lesser extent (010)[100] slip systems. Somewhat similar CPOs formed under hydrous conditions in the torsion experiments of Demouchy et al. (2012) at  $\gamma \approx 2$ , although the bimodal distributions are less distinct than in the experiments of Tasaka et al. (2016), potentially due to the lower shear strains achieved and/or partial dehydration. The bimodal CPO may provide a new microstructural indicator of deformation of olivine with elevated concentrations of hydrous point defects and has implications for the physical properties of the rock, including seismic wave velocities and anisotropy.

An olivine CPO that is strikingly similar to those produced in the experiments of Tasaka et al. (2016) was reported by Mercier and Carter (1985) to be present in a sheared lherzolite xenolith (PHN1611) from the 90 Ma Thaba Putsoa kimberlite, Lesotho (Nixon and Boyd, 1973; Allsopp et al., 1989). Thermobarometric estimates indicate that the xenolith was extracted from a depth with temperature and pressure in the ranges 1420–1470 °C and 5.4–6.9 GPa (~170–210 km depth) (Carswell, 1991; Pearson et al., 1995; Tharimena et al., 2017), typical of sheared xenoliths hosted in kimberlites from across South Africa (Tharimena et al., 2017). The olivine CPO of PHN1611 exhibits bimodal maxima of [100] and [001] axes at 45° to the shear direction and shear plane normal inferred from the microstructure, whilst [010] axes form a single maximum perpendicular to the [100] and [001] maxima (Mercier and Carter, 1985). Mercier and Carter (1985) were unable to explain the formation of this unusual CPO due to a lack of contemporary experimental analogues. However, the recent experimental results of Tasaka et al. (2016) indicate that the olivine CPO of PHN1611 is potentially related to elevated concentrations

of hydrous point defects, in which case the xenolith supports the relevance of the experimental results to natural deformation.

In this study, we employ a range of techniques to investigate the role of water in the development of the observed bimodal CPO in olivine. First, we characterise the microstructure and CPO of PHN1611 using electron backscatter diffraction (EBSD), to confirm the presence of the bimodal olivine CPO in our sample. Then, we employ two approaches to test the hypothesis that bimodal CPOs form as a result of deformation dominated by activity of the (001)[100] and (100)[001] slip systems. First, we use high-angular resolution electron backscatter diffraction (HR-EBSD) to map the densities of different types of geometrically necessary dislocations (GNDs) in olivine deformed experimentally under anhydrous (Hansen et al., 2012) and hydrous (Tasaka et al., 2016) conditions, as well as in PHN1611 (Mercier and Carter, 1985). Second, we employ visco-plastic self-consistent (VPSC) simulations of CPO development in olivine to characterise the effects of varying the strengths of the (001)[100] and (100)[001] slip systems relative to (010)[100]. We also report secondary ion mass spectrometry (SIMS) measurements of water content in PHN1611 to test the hypothesis that development of the bimodal CPO of olivine within it is related to elevated concentrations of intracrystalline hydrous point defects. Lastly, we assess the impact of the bimodal CPO of olivine in PHN1611 on seismic wave velocities and anisotropy in the mantle.

## 2. Methods

### 2.1. Experimental procedures

We utilise samples of polycrystalline, iron-rich olivine ( $\text{Fo}_{50}$ ) that were deformed experimentally under anhydrous (sample PT-0457) and water-saturated (sample PT-0966) conditions. Whereas magnesium-rich olivine ( $\text{Fo}_{90}$ ) is typical of the upper mantle, the lower strength of  $\text{Fo}_{50}$  reduces the risk of slip at the piston-sample interfaces during torsion experiments. Iron content does not dramatically affect the relative strengths of different slip systems in olivine (Kohlstedt and Ricoult, 1984) and consequently CPO evolution in aggregates of anhydrous  $\text{Fo}_{50}$  and  $\text{Fo}_{90}$  is statistically indistinguishable (Hansen et al., 2014).

Both experimental samples are thin-walled cylinders that were deformed in torsion in a servo-controlled gas-medium apparatus at the University of Minnesota at 1200 °C and a confining pressure of  $300 \pm 2$  MPa. Sample PT-0457 was deformed under controlled stress of 166 MPa to a finite shear strain ( $\gamma$ ) of 5.4 (Hansen et al., 2012). The macroscopic shear-strain rate varied from  $6 \times 10^{-4}$  to  $7 \times 10^{-3} \text{ s}^{-1}$ . Stress-stepping tests revealed a stress exponent of  $n = 3.7$  for this sample. Based on observed strain localisation within fine grained regions in multiples samples, Hansen et al. (2012) inferred dislocation-accommodated grain boundary sliding to be the dominant deformation mechanism in these experiments. Sample PT-0966 was deformed to  $\gamma = 5.0$ , and its microstructure is assumed to have reached steady state under the final equivalent stress of 80 MPa and strain rate of  $1 \times 10^{-3} \text{ s}^{-1}$  (Tasaka et al., 2016). Talc, encapsulated in the centre of the sample and dehydrating throughout the experiment, was used to maintain water-saturated conditions. Fourier transform infrared spectra collected after the experiment from the PT-0966  $\text{Fo}_{50}$  aggregate indicate a water-content of 1160 ppm H/Si, whereas a large single crystal of San Carlos olivine embedded within the  $\text{Fo}_{50}$  has a water-content of 333 ppm H/Si (calibration of Paterson, 1982), confirming water-saturation (Tasaka et al., 2016). These observations are consistent with the increasing solubility of H in olivine with increasing Fe-content (Zhao et al., 2004; Withers et al., 2011). A broad peak in FTIR spectra from the  $\text{Fo}_{50}$  aggregate indicates the presence of free water as bubbles and corroborates that the sample remained

**Table 1**  
Details of EBSD maps and acquisition settings.

Specimen	Purpose	Map grid dimensions (points)	Step size ( $\mu\text{m}$ )	Pixels in diffraction patterns
PHN1611	Bulk characterisation	2476 $\times$ 2552	6.29	168 $\times$ 128
PHN1611	HR-EBSD	400 $\times$ 270	2.5	627 $\times$ 512
PT-0457	HR-EBSD	500 $\times$ 375	0.2	627 $\times$ 512
PT-0966	HR-EBSD	680 $\times$ 460	0.5	627 $\times$ 512

water-saturated throughout the experiment (Karato et al., 1986; Tasaka et al., 2016). Based on mechanical data (stress exponents  $\approx 5.0$  and grain size exponent  $\approx 0$ ) and microstructural observations, Tasaka et al. (2016) inferred that these samples deformed by dislocation creep. They observed a pronounced evolution of mechanical properties and CPO with increasing shear strain. Therefore, we analysed the microstructure of their highest strain sample deformed to a shear strain of 5.0, by which point steady state creep was well established.

## 2.2. Specimen preparation for microstructural characterisation

Experimental samples deformed in torsion were cut parallel to the torsion axis, near the external margin of the cylinder to reveal tangential sections. Xenolith sample PHN1611 was received sectioned perpendicular to the foliation defined by alignment of pyroxene porphyroclasts and bands of dynamically recrystallised grains. All samples were polished with a range of increasingly fine diamond grits and finished by polishing with 0.04  $\mu\text{m}$  colloidal silica.

## 2.3. Electron backscatter diffraction data acquisition

EBSD in the scanning electron microscope (SEM) was used to analyse mineral phase and orientation. EBSD data were acquired using Oxford Instruments Aztec 2.1 software on FEI Quanta 650 field-emission gun SEMs equipped with Oxford Instruments NordlysNano and Nordlys-S EBSD cameras in the Department of Earth Sciences, University of Oxford, and the School of Earth and Environment, University of Leeds. Map details and acquisition settings are summarised in Table 1. Data were collected at 70° specimen tilt, 8.1–10.1 mm working distance, and 20–30 kV accelerating voltage.

Prior to acquisition of datasets intended for HR-EBSD post-processing, an automated calibration routine was performed to determine the position of the pattern centre (the point on the phosphor screen of the EBSD detector that is closest to the point where the electron beam is incident on the specimen surface) specific to each dataset. This routine collects electron backscatter patterns (EBSPs) with the EBSD detector inserted to different insertion distances spread at 4 mm intervals over 20 mm. Cross-correlation of these EBSPs is used to determine the pattern centre prior to each EBSD run. Accurate calibration of the pattern centre is necessary to allow for correction during HR-EBSD post-processing of pattern shifts due to beam scanning.

## 2.4. High-angular resolution electron backscatter diffraction data processing

To map the densities and distributions of different types of dislocation in olivine, we used HR-EBSD. This method was developed in the materials sciences (Wilkinson et al., 2006; Wilkinson and Randman, 2010; Britton and Wilkinson, 2011) and was recently adapted to olivine and quartz by Wallis et al. (2016, 2017b). Although conventional EBSD can measure lattice misorientation angles to approximately 0.2°, its precision is limited by determining

band positions in Hough-space. In contrast, HR-EBSD utilises cross-correlation of typically 100 regions of interest within stored EBSPs to achieve measurements of lattice misorientation with precision on the order of 0.01° (Wilkinson et al., 2006; Britton and Wilkinson, 2011). Furthermore, conventional EBSD suffers from large uncertainty in the misorientation axis when the misorientation angle is only a few degrees or less (Prior, 1999). In contrast, HR-EBSD can achieve precision in misorientation axes of a few degrees for misorientation angles of 1.0° or less (Wilkinson, 2001). As a result of this precision in both misorientation angles and axes, lattice orientation gradients measured by HR-EBSD can be used to precisely determine components of the Nye tensor, which describe the densities of specific types of geometrically necessary dislocations (GNDs) (Nye, 1953; Wilkinson and Randman, 2010). Due to the limited number of slip systems in olivine, a single best-fit solution can be found for the densities of six principle dislocation types following the method of Wallis et al. (2016). This approach assumes that distortion due to long-range elastic strain gradients is negligible compared to that arising from GND content (Wilkinson and Randman, 2010) and has been used to estimate GND densities in olivine single crystals and polycrystalline aggregates (Wallis et al., 2016, 2017a). HR-EBSD also maps elastic strain (Wilkinson et al., 2006), and demonstrates that this assumption is reasonable for our samples, in which the strain gradients across subgrain boundaries are typically <5% of the orientation gradients.

Noise in the GND density estimates arises due to noise in the measured orientation gradients and depends on individual grain orientations and the mapping step size (Wallis et al., 2016). For example, when the Burgers vector of an edge dislocation is approximately normal to the plane of the map, little of the lattice curvature that it generates is observable. Therefore, high densities of such a dislocation type are required to fit spurious orientation gradients that arise from orientation noise (Wallis et al., 2016). This effect manifests as uniformly high background GND densities (e.g.,  $>10^{14} \text{ m}^{-2}$ ) for one or more dislocation types in some grains occupying particular orientations (e.g., [001] normal to the plane of the map). The ability to resolve orientation gradients also depends on the distance over which the gradient is measured, i.e., the mapping step size. Maps of the noise floor for each dislocation type in each grain in each sample, estimated based on the angular resolution, step size, and crystal orientation, are given in the Supplementary Material. Our analysis focuses on the relative abundances of subgrain boundaries containing each dislocation type, which manifest as linear structures with GND densities elevated above the background level (either the noise floor or more distributed dislocation content) in each grain. Compared to conventional EBSD, the improved angular resolution of HR-EBSD serves to lower the GND density noise floors and therefore reveals a greater proportion of the subgrain boundaries, providing more complete representations of the dislocation content.

## 2.5. Secondary ion mass spectrometry

Measurements of water concentration in clinopyroxene grains from PHN1611 were used to estimate water concentration in olivine. This approach was taken because olivine commonly loses water by diffusion during uplift and/or exposure, whereas pyrox-

enes generally retain water concentrations consistent with those expected under mantle conditions (e.g., Warren and Hauri, 2014). Measurements were made using the Cameca IMS 6f Secondary Ion Mass Spectrometer at the Carnegie Institution of Washington following the methods and processing detailed in Kumamoto et al. (2017). Pyroxene grains were mounted in indium metal and polished with SiC sandpaper and diamond suspensions down to 1  $\mu\text{m}$  grit size. After gold-coating, the mount was placed in the exchange chamber of the SIMS for 24 h before being moved into the analysis chamber in order to maintain ultrahigh vacuum ( $P < 10^{-9}$  torr). Analyses were made using a rastered  $\text{Cs}^+$  beam with a current of 15–25 nA. An electron flood gun was used to charge balance the sample. Background water concentrations were measured on Suprasil 3002 glass, and instrument drift was tracked using measurements of ALV-519-4-1 basaltic glass. Calibration curves were constructed using standards calibrated by Koga et al. (2003) and Aubaud et al. (2007). We use the experimentally derived partition coefficient of  $D^{\text{O/Cpx}} = 0.07$  (Hauri et al., 2006; Tenner et al., 2009; O’Leary et al., 2010) to estimate the concentration of water in olivine.

## 2.6. Visco-plastic self-consistent simulations

To investigate the control exerted by relative slip system strengths on the development of CPO, we employed VPSC simulations of polycrystal deformation (Lebensohn and Tomé, 1993). VPSC simulations provide the opportunity to investigate CPOs developed by slip systems with a wide range of relative strengths and thereby assess whether those slip systems inferred from microstructural observations of the experimental and natural samples are capable of producing the bimodal CPO. This approach determines the shear rate ( $\dot{\gamma}^s$ ) on each slip system ( $s$ ) to calculate the strain rate tensor ( $\dot{\epsilon}$ ) of each grain in response to a deviatoric stress tensor ( $\sigma'$ ) imposed by the surrounding medium. As a simplifying assumption, the mechanical properties of the polycrystalline matrix surrounding each grain are averaged to provide an ‘effective homogeneous medium’, against which each grain is considered in turn (a ‘mean-field’ approach). Eshelby theory, modified for visco-plasticity, is used to solve for a self-consistent mechanical state in each grain at each deformation step (Lebensohn and Tomé, 1993). After each deformation step, grain orientations are updated according to the lattice rotation rate ( $\dot{\omega}_{ij}$ ) determined by

$$\dot{\omega}_{ij} = \dot{\Omega}_{ij} + \Pi_{ijkl} S_{klmn}^{-1} \tilde{\epsilon}_{mn} - \sum_s \frac{1}{2} (b_i n_j - b_j n_i)^s \dot{\gamma}^s \quad (1)$$

where  $\dot{\Omega}$  is the antisymmetric component of the macroscopic distortion rate,  $\mathbf{S}$  is the visco-plastic Eshelby tensor,  $\tilde{\epsilon}$  is the strain rate deviation in the grain from the polycrystal average, and  $\mathbf{b}$  and  $\mathbf{n}$  are the Burgers vector and slip plane normal (Lebensohn and Tomé, 1993). The shear rate ( $\dot{\gamma}^s$ ) on each slip system is computed by

$$\dot{\gamma}^s = \dot{\gamma}_0 \left( \frac{m_{ij}^s \sigma'_{ij}}{\tau_c^s} \right)^n \quad (2)$$

where  $\dot{\gamma}_0$  is a reference shear rate,  $\mathbf{m}$  is the Schmid tensor,  $n$  is the stress exponent, and  $\tau_c^s$  is the critical resolved shear stress to initiate dislocation motion on slip system  $s$  (Lebensohn and Tomé, 1993). We set  $n = 3.5$ , based on experiments on single crystals of San Carlos olivine (Bai et al., 1991), although the value of  $n$  does not affect the CPO evolution. The relative values of  $\tau_c^s$  are varied between 1 and 10 to simulate changing relative slip system strengths (Lebensohn and Tomé, 1993; Tommasi et al., 2000). We employed the ‘second-order’ method (Liu and Ponte Castañeda,

2004; Castelnau et al., 2008) to provide a linear approximation of the non-linear behaviour of olivine and to incorporate the effects of stress heterogeneity within grains.

To establish the relative strengths of each slip system that controls the development of the unusual CPO in the water-saturated experimental samples and the xenolith, we explored the effects of varying  $\tau_c^s$  for each slip system. We consider the slip systems active during high-temperature creep of olivine following Tommasi et al. (2000). Tasaka et al. (2016) inferred that CPO development was controlled by competition between slip on (010)[100], (001)[100], and (100)[001]. Therefore, to identify a combination of slip system strengths that reproduces the observed CPO, we initially tested the effect of setting  $\tau_c^{(001)[100], (100)[001]} = 1$ , varying  $\tau_c^{(010)[100]}$  between 1–10, and setting  $\tau_c^{\text{othersystems}} = 10$ . The other slip systems included are (010)[001], {011}[100], {031}[100], {110}[001], and {111}[1 $\bar{1}0$ ]. The (010)[001] system is relatively strong under relevant conditions (Mackwell et al., 1985; Bai et al., 1991; Raterron et al., 2012); {011}[100], {031}[100], and {110}[001] are infrequently observed (Darot and Gueguen, 1981; see Table 1 of Tommasi et al., 2000, for a review); and {111}[1 $\bar{1}0$ ] is included to fulfil the von Mises criterion requiring five independent slip systems to accommodate any arbitrary deformation (Castelnau et al., 2008). All simulations started with the same set of 500 random grain orientations. A velocity gradient tensor for simple shear, consistent with the known kinematics of the experiments and the inferred kinematics of the natural deformation, was imposed and simulations were run to  $\gamma = 5$  to match the experiments.

## 2.7. Estimation of seismic properties

To quantify the impact of the olivine CPO in PHN1611 on the seismic properties of mantle rocks, we employed calculations based on the EBSD measurements of its CPO and effective-medium theory. For each measurement point in the map in Fig. 2, the elastic stiffness tensor of the mineral (Bass, 1995) was rotated into the sample reference frame according to the measured crystal orientation. Effective-medium theory was used to compute the Hill average of the Voigt and Reuss bounds on the elastic properties of the aggregate of each mineral from the rotated stiffness tensors. Analyses of the Finero peridotite by Zhong et al. (2014) demonstrated that wave velocities predicted from the Hill average were within 0.2  $\text{km s}^{-1}$  of those from the Voigt and Reuss bounds and were in excellent agreement with seismic velocities predicted by a finite-element simulation and with laboratory measurements. Moreover, the Hill average provided an excellent estimate of the magnitude of anisotropy. The average of the aggregate stiffness tensors, weighted by the area fraction of each mineral, was computed to estimate the elastic properties of the bulk rock. Calculations were performed using the MTEX toolbox (Mainprice et al., 2011) for MATLAB®.

## 3. Results

### 3.1. Xenolith microstructure

In the EBSD map of PHN1611 in Fig. 2, the microstructure is characterised by a matrix of olivine ( $\text{Fo}_{87}$ ) (60% of indexed points) containing porphyroclasts of orthopyroxene (12%), clinopyroxene (13%), and garnet (15%) (Fig. 2a). Pyroxene porphyroclasts are commonly rimmed by mantles of finer-grained pyroxene interpreted to result from dynamic recrystallisation. The garnets have kelyphitic overgrowths of predominantly orthopyroxene and clinopyroxene. These fine-grained rims on pyroxenes and garnets merge into through-going layers typically  $< 100 \mu\text{m}$  thick that dissect the olivine matrix. The intervening olivine domains vary in thickness, between one and approximately 10 olivine grains. Olivine exhibits a pronounced CPO (Fig. 2b). Its [010] axes form a single maximum,



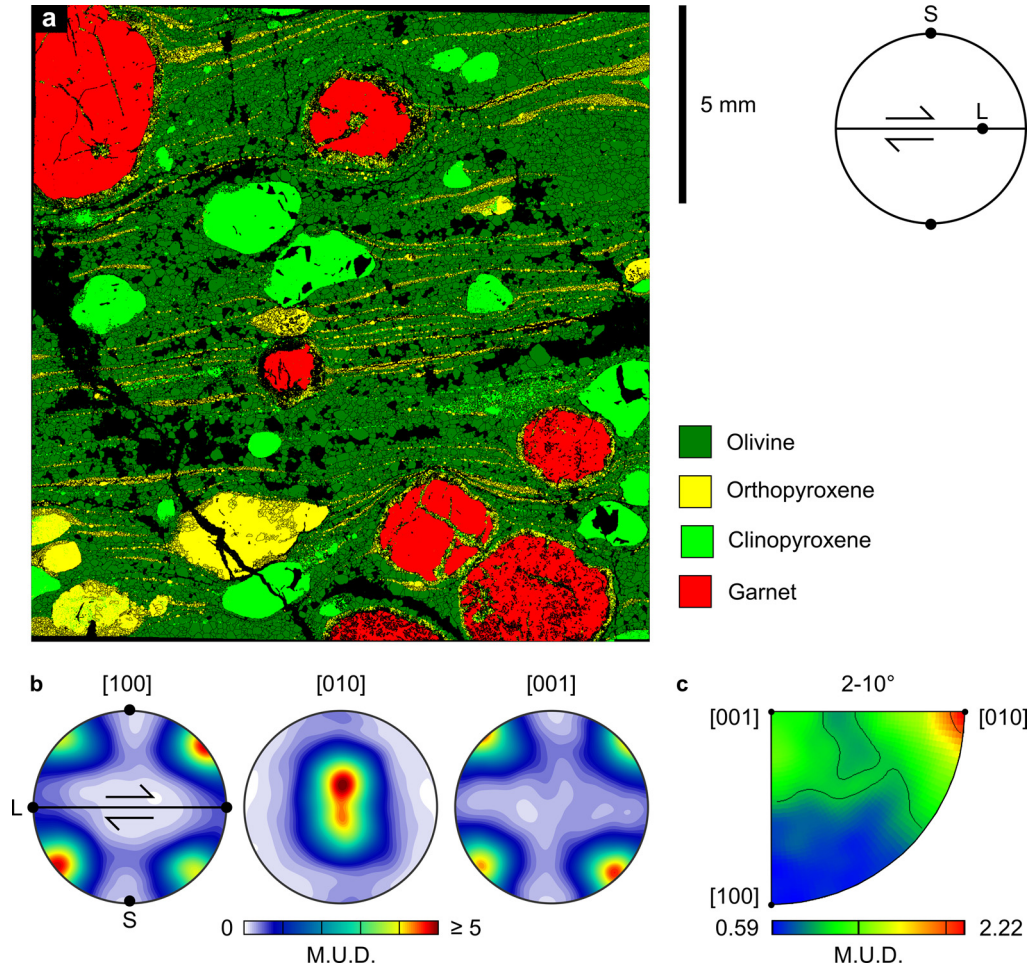


**Fig. 2.** Microstructural data from EBSD mapping of xenolith sample PHN1611. (a) Phase map. Black lines indicate grain boundaries of  $\geq 10^\circ$  misorientation, and black areas indicate unindexed regions. (b) Pole figures of olivine crystal orientations. S and L indicate the foliation normal and lineation, the latter inferred by comparing the CPO to the measurements of Mercier and Carter (1985). (c) Inverse pole figure of misorientation axes of subgrain boundaries in olivine. Misorientation axes for subgrain boundaries with misorientation angles in the range  $2\text{--}10^\circ$  are plotted. The pole figures and misorientation inverse pole figure are coloured by multiples of uniform distribution (M.U.D.).

whilst [100] and [001] axes both form pairs of orthogonal maxima. To correct for misalignment of the section relative to the shear direction, the orientation data are rotated  $40^\circ$  about a vertical axis to match the CPO of PHN1611 reported by Mercier and Carter (1985). As such, the [010] maximum is perpendicular to the shear direction and shear plane normal, whereas the [100] and [001] maxima bisect the shear direction and shear plane normal (Fig. 2b). The misorientation axes of subgrain boundaries in olivine, with misorientation angles in the range  $2\text{--}10^\circ$ , form maxima parallel to [010] and to a lesser extent [001] (Fig. 2c).

### 3.2. Geometrically necessary dislocations

Densities of GNDs in the anhydrous Fo<sub>50</sub> sample, PT-0457, are presented in Fig. 3. Subgrain boundaries, evident as linear arrays of elevated GND density, typically appear approximately straight and vertical, and are composed primarily of (010)[100] and (001)[100] edge dislocations. Subgrain boundaries containing edge dislocations with [001] Burgers vectors and screw dislocations are less abundant. Background GND densities within subgrain interiors are at or near the noise floor. Noise floors for (100)[001] edge dislocations are particularly low, and it is clear that very few of the subgrain boundaries contain this dislocation type.

Densities of GNDs in the hydrous Fo<sub>50</sub> sample, PT-0966, are presented in Fig. 4. A complex network of subgrain boundaries is present and contains contributions from all dislocation types.

Edge dislocations with [100] Burgers vectors (both (010)[100] and (001)[100]) are most common within the subgrain boundaries but those with [001] Burgers vectors also make a significant contribution.

Densities of GNDs in the xenolith, PHN1611, are presented in Fig. 5. Subgrain boundaries are present within most grains. Subgrain boundaries are composed of a range of dislocation types, including both edge and screw character, except (010)[001] edge dislocations, which make only rare contributions. (010)[100], (001)[100], and (100)[001] edge dislocations are present in approximately equal proportions.

### 3.3. Water concentrations in xenolith PHN1611

SIMS analysis of clinopyroxene in PHN1611 revealed an average hydrogen concentration of  $260 \pm 45$  ppm H<sub>2</sub>O. Based on the experimentally derived partition coefficient of  $D^{\text{Ol/Cpx}} = 0.07$  (Hauri et al., 2006; Tenner et al., 2009; O'Leary et al., 2010) and scaled to the Paterson (1982) FTIR calibration, this water concentration in clinopyroxene corresponds to an average concentration of  $100 \pm 20$  ppm H/Si in olivine. This water content is intermediate between those of the Fo<sub>50</sub> in PT-0457 ( $\approx 0$  ppm H/Si, Hansen et al., 2012) and PT-0966 (1160 ppm H/Si, Tasaka et al., 2016), and is typical of exhumed mantle peridotites (Peslier, 2010; Warren and Hauri, 2014).



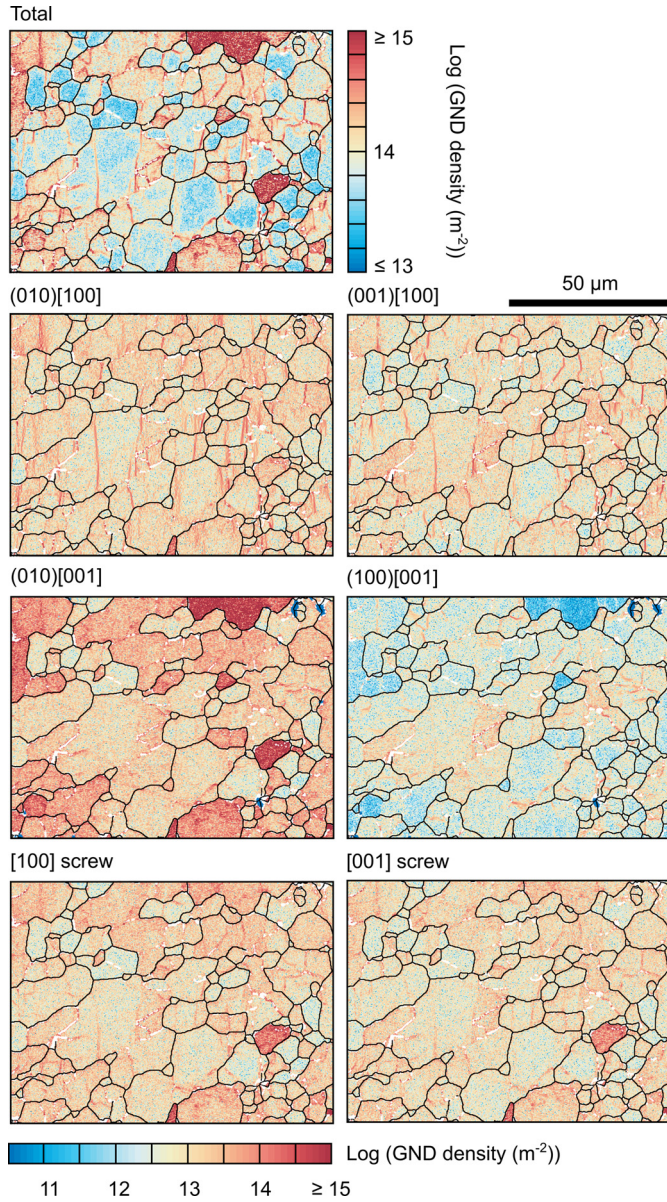


**Fig. 3.** Densities of geometrically necessary dislocations (GNDs) in anhydrous Fo<sub>50</sub> olivine (PT-0457) deformed in torsion (top-to-right) to shear strain  $\gamma = 5.4$  at 1200 °C and an equivalent stress of 166 MPa. Black indicates grain boundaries and white indicates areas without reliable measurements.

### 3.4. Visco-plastic self-consistent simulations

Fig. 6 presents the results of VPSC simulations in which the relative strength of the (010)[100] slip system was varied between 1 and 10, whereas (001)[100] and (100)[001] were kept weak (relative strengths of 1) and all other slip systems were kept strong (relative strengths of 10). The CPOs formed at  $\gamma = 5$  are displayed in each case. The CPOs exhibit systematic variations as the relative strength of (010)[100] is increased. When (010)[100] is as weak as (001)[100] and (100)[001], single maxima of [100] and [001] axes develop at less than approximately 30° to the shear direction. The [010] axes form a maximum parallel to the shear plane normal and are girdled normal to the shear direction. In contrast, when (010)[100] is 10 times stronger than (001)[100] and (100)[001] (and therefore similar to all other slip systems), the CPO developed is markedly different. [100] and [001] axes form pairs of orthogonal maxima at 45° to the shear direction and the shear plane normal. [010] axes form a maximum perpendicular to both

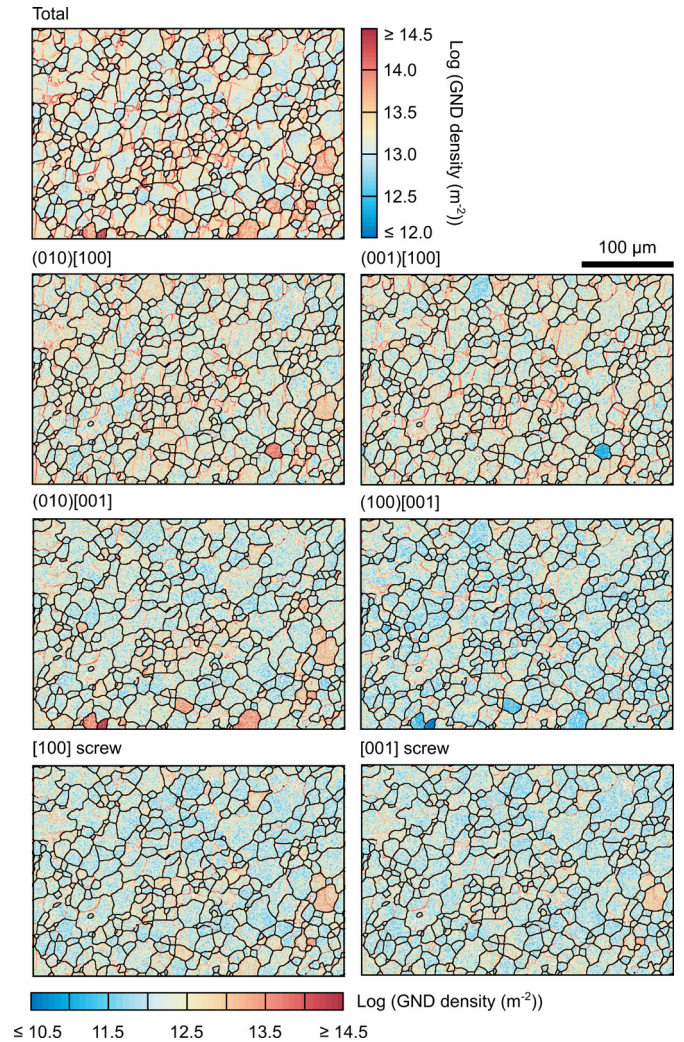


**Fig. 4.** Densities of geometrically necessary dislocations (GNDs) in hydrous Fo<sub>50</sub> olivine (PT-0966) deformed in torsion (top-to-right) to shear strain  $\gamma = 5.0$  at 1200 °C and a final stress of 80 MPa. Black indicates grain boundaries and white indicates areas without reliable measurements.

the shear direction and shear plane normal, and are weakly girdled parallel to the shear plane.

The CPO formed when (010)[100] has a relative strength of 5 has most similarity to those of the xenolith and the hydrous Fo<sub>50</sub> sample insofar as one [100] maximum is slightly stronger than the other and the [010] axes display the least girdling. Therefore, we present the evolution of this CPO with increasing strain in more detail in Fig. 7. From an initially random distribution of crystal orientations, [100] and [001] axes develop two weak maxima of similar strength and [010] axes develop a weakly girdled maximum by  $\gamma = 2-3$ . By  $\gamma = 4-5$  the different strengths of the [100] maxima are established and the girdling of the [010] maximum is reduced. [001] axes maintain double maxima of similar strength from  $\gamma = 2$  onwards. At  $\gamma = 5$ , the relative slip system activities, normalised by the number of symmetrically equivalent variants, are all below 0.024, except for (001)[100] and (100)[001], which both have activities of 0.236.

### 3.5. Seismic properties

Fig. 8 presents seismic wave velocities and their anisotropy estimated from the EBSD map of PHN1611 (Fig. 2). To assess the control exerted by olivine on the bulk-rock properties, we present the results of calculations based on olivine only and also includ-



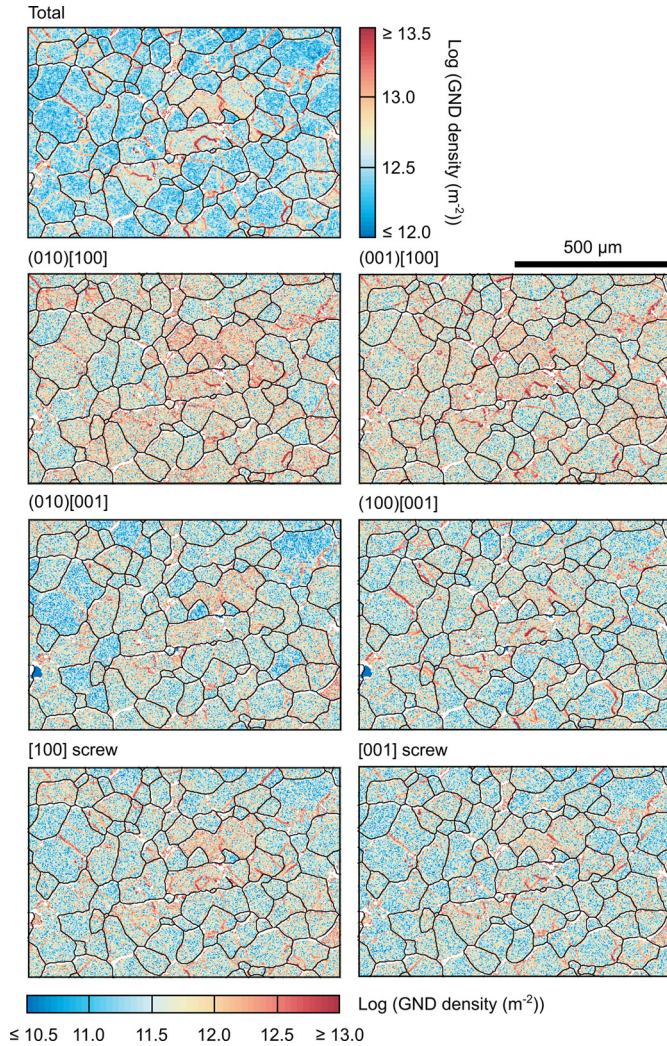


**Fig. 5.** Densities of geometrically necessary dislocations (GNDs) in xenolith sample PHN1611. Black indicates grain boundaries and white indicates areas without reliable measurements.

ing all the major minerals (olivine, orthopyroxene, clinopyroxene, and garnet). The general distributions of velocities are similar in both cases. Primary and secondary maxima in P-wave velocity ( $V_p$ ) coincide with the primary and secondary maxima in the distributions of olivine [100] axes (Fig. 2c). Maxima in the velocity of the fast shear wave ( $V_{s1}$ ) occur between the maxima in  $V_p$  and are aligned with the inferred bulk-rock shear direction and shear plane normal. The velocity of the slow shear wave ( $V_{s2}$ ) varies little compared to  $V_{s1}$ . As such, the directional dependence of the difference in velocity between  $V_{s1}$  and  $V_{s2}$  (i.e.,  $AVs$ ) reflects the distribution of  $V_{s1}$ . Despite the general similarities in the distributions, the magnitudes of the seismic wave velocities are lower in the estimates based on the full major mineral assemblage than based on olivine alone. The inclusion of other minerals reduces  $V_p$  from approximately 9.1–10.0  $\text{km s}^{-1}$  to 7.6–8.3  $\text{km s}^{-1}$  and reduces  $V_{s1}$  from 5.5–5.9  $\text{km s}^{-1}$  to 4.6–4.9  $\text{km s}^{-1}$ .  $V_{s2}$  and  $AVs$  are also reduced.

#### 4. Discussion

##### 4.1. Slip systems involved in development of the bimodal crystallographic preferred orientation

The bimodal CPO of olivine in xenolith PHN1611, recorded by Mercier and Carter (1985), has remained unexplained due to its

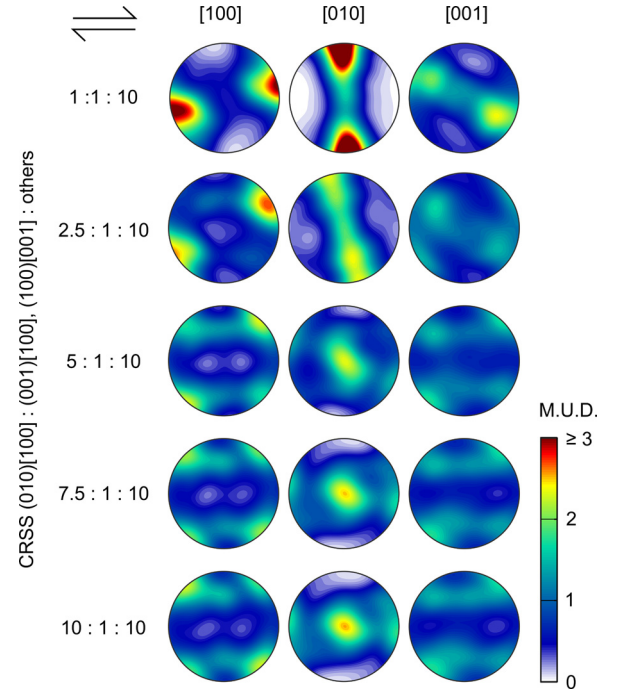


**Fig. 6.** Pole figures of results from VPSC simulations with varying CRSS for (010)[100]. In each simulation the relative CRSSs of (001)[100] and (100)[001] are held constant at 1. The relative CRSS of (010)[100] is varied between 1 and 10. The CRSSs of all other slip systems are held constant at 10. Results are plotted at a shear strain of 5.

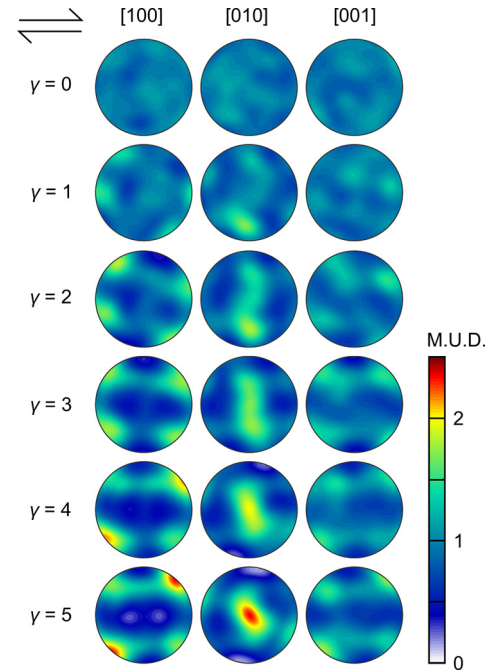


**Fig. 7.** Pole figures of results from a VPSC simulation, at shear strains between 1 and 5, with the CRSS ratios of slip systems held constant. The relative CRSSs of (001)[100] and (100)[001] are 1, that of (010)[100] is 5, and those of all other slip systems are 10.

different characteristics from other naturally occurring (e.g., Ben Ismail and Mainprice, 1998) and experimentally generated (e.g., Jung et al., 2006) olivine CPOs. Early hypotheses regarding its formation included the possibility that the bimodal CPO was generated by paramorphosis transformation from twinned high-pressure polymorphs via mechanisms similar to those described by Kerschhofer

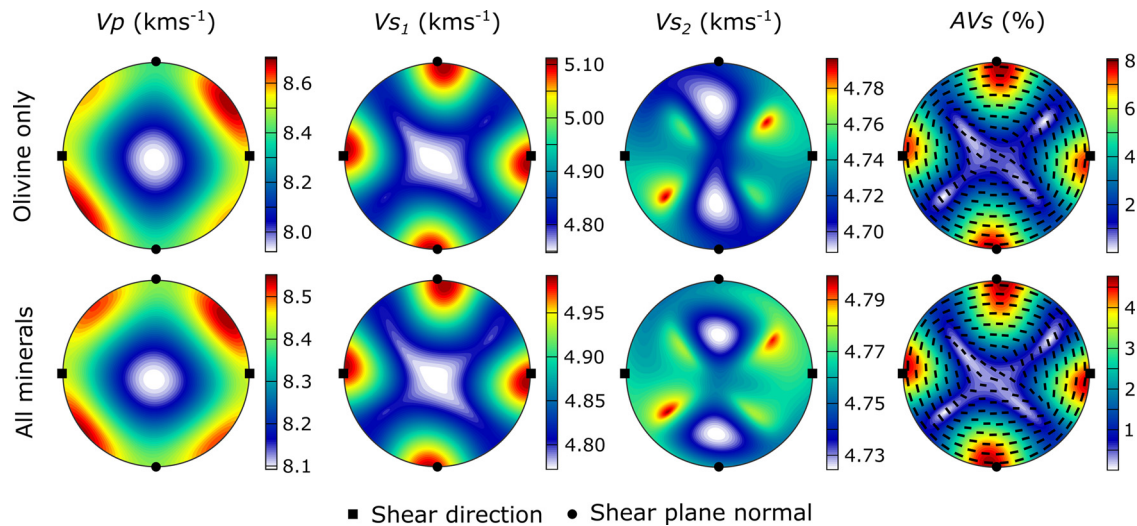


**Fig. 8.** Seismic properties of peridotite xenolith PHN1611 estimated from EBSD data. Seismic wave velocities and their anisotropy are calculated based on olivine only (top) and inclusion of all major minerals (bottom).  $V_p$  is the velocity of the primary (longitudinal) wave,  $V_{s1}$  is the velocity of the fast secondary (shear) wave,  $V_{s2}$  is the velocity of the slow secondary (shear) wave, and  $AV_s$  is the difference in velocity of the differently polarised (fast and slow) shear waves. Tick marks indicate the polarisation direction of the fast shear wave.

et al. (1996) (D. Mainprice, pers. com., 1997). However, the new EBSD data in Fig. 2a reveals that boundaries with misorientations of  $90^\circ$  about [010] (within a tolerance of  $3^\circ$ ) constitute only 0.05% of olivine grain boundaries. This lack of consistent orientation relationships, the highly strained microstructure, and chemical equilibration at pressures of  $<7$  GPa (Carswell, 1991; Pearson et al., 1995) militate against a transformation or twinning origin for the CPO of PHN1611. Instead, comparison to the recent experiments of Tasaka et al. (2016) and predictions of VPSC simulations indicate that the bimodal CPO results from activation of a particular combination of slip systems. Based on mechanical data from experiments, the CPO, and misorientation analysis of subgrain boundaries, Tasaka et al. (2016) inferred that the bimodal CPO formed during dislocation creep dominated by the (001)[100], (100)[001], and (010)[100] slip systems. The improved precision in misorientation angles and axes provided by HR-EBSD allows us to interrogate the substructure in more detail by analysing the densities and types of geometrically necessary dislocations present in the samples. A particular advantage of HR-EBSD for the present study is the ability to discriminate between (001)[100] and (100)[001] edge dislocations based on the different lattice curvatures that they generate.

Subgrain boundaries in the sample of anhydrous  $\text{Fo}_{50}$  olivine deformed in torsion to  $\gamma = 5.4$  at  $1200^\circ\text{C}$  (Hansen et al., 2012) are predominantly tilt walls composed of (010)[100] and/or (001)[100] edge dislocations (Fig. 3). Relatively few of the subgrain boundaries contain GNDs with [001] Burgers vectors. These observations are consistent with previous interpretations based on CPO development (e.g., Zhang and Karato, 1995; Tommasi et al., 2000; Hansen et al., 2012), misorientation analysis of subgrain boundaries using conventional EBSD (e.g., Hansen et al., 2014), and experimental observations that slip systems with [100] Burgers vectors are weakest in anhydrous olivine at high temperatures (e.g., Raleigh, 1968; Bai et al., 1991). The sample of water-saturated  $\text{Fo}_{50}$  olivine deformed in torsion to  $\gamma = 5.0$  at  $1200^\circ\text{C}$  (Tasaka et al., 2016) also contains a predominance of edge dislocations with [100] Burgers vectors within the subgrain boundary network (Fig. 4). However, in contrast to the anhydrous sample, the water-saturated olivine also exhibits numerous subgrain boundaries containing GNDs with [001] Burgers vectors (Fig. 4). The presence of (100)[001] edge dislocations is consistent with the interpretations of Tasaka et al. (2016), as well as previous work on  $\text{Fo}_{90}$  with elevated wa-

ter contents deformed to lower strains (Jung and Karato, 2001; Jung et al., 2006). The xenolith exhibits approximately equal numbers of subgrain boundaries containing (010)[100], (001)[100], and (100)[001] edge dislocations, whereas (010)[001] edge dislocations make only rare contributions (Fig. 5). In summary, the principle difference in GND content between the anhydrous experimental sample, the xenolith, and the water-saturated experimental sample is the greater prevalence of (100)[001] edge dislocations in the latter samples, both of which exhibit the bimodal CPO.

To assess the CPO produced by the slip systems inferred to be important from the GND density analysis, we consider the results of the VPSC simulations (Figs. 6 and 7). The microstructural data of Tasaka et al. (2016) and the results of our GND analysis above indicate that the (001)[100], (100)[001], and (010)[100] slip systems potentially play a role in formation of the bimodal CPO. Fig. 6 indicates that when these slip systems are equally weak relative to the other slip systems a CPO develops with single maxima of [100] and [001] axes at low angles to the shear direction. However, when (001)[100] and (100)[001] are  $\geq 5$  times weaker than (010)[100] (and the other slip systems) the bimodal CPO develops (Fig. 6). The simulation for which (001)[100] and (100)[001] are 5 times weaker than (010)[100] most closely matches the CPO of the water-saturated experimental sample (Fig. 1) and the xenolith (Fig. 2), insofar as the [100] maxima have unequal strengths and the [010] axes exhibit the least girdled distribution parallel to the shear plane (Fig. 6). In this simulation, the bimodal distributions of [100] and [001] axes begin to develop at  $\gamma = 1$ –2, and [010] axes exhibit distributions that are somewhat girdled normal to the shear direction at  $\gamma = 2$ –3, before establishing a stronger point maximum at higher shear strains (Fig. 7). This CPO evolution is remarkably similar to that observed in the experiments of Tasaka et al. (2016) (their Fig. 5) and is interpreted to result from competition between slip systems. There is a difference in the orientation of the dominant [100] maximum developed in the experiments of Tasaka et al. (2016) (Fig. 1) compared to that observed in the xenolith (Fig. 2) and the VPSC simulations (Figs. 6 and 7). The VPSC simulations in Fig. 6 indicate that this difference is due to slight differences in relative slip systems strengths, with easier slip on systems with [100] Burgers vectors generally reducing the angle between the [100] maximum and the shear direction. This explanation is consistent with the wide body of work on the role of relative slip system activities in generating the variety of CPO types



found in experimental and natural samples (e.g., Jung et al., 2006; Bernard and Behr, 2017). Overall, the combined results of GND analysis and VPSC simulations support the interpretation of Tasaka et al. (2016) that the bimodal CPO results from grain rotations being controlled by activity of the (001)[100] and (100)[001] slip systems, with a more minor contribution from (010)[100]. Moreover, GND analysis of the xenolith indicates that the interpretations of experiments by Tasaka et al. (2016) also provide a plausible explanation of development of bimodal CPO during deformation under natural conditions.

#### 4.2. Impact of water on slip system activity

The findings of this study and that of Tasaka et al. (2016), regarding the development of the bimodal CPO, are broadly consistent with the findings of previous studies regarding the impact of water on the development of different types of unimodal CPO. Olivine with low concentrations of intracrystalline hydrous point defects typically forms an A-type CPO, with single maxima of [100] axes and [010] axes respectively parallel to the shear direction and shear plane normal (Fig. 1). This CPO is inferred to result from deformation dominated by the (010)[100] slip system in both experiments and nature (e.g., Zhang and Karato, 1995; Jung et al., 2009; Hansen et al., 2014; Cao et al., 2015) (Fig. 1). In contrast, olivine with elevated concentrations of hydrous point defects typically develops a CPO characterised by single maxima of crystal axes in orientations that indicate a dominance of one of the slip systems (001)[100], (100)[001], or (010)[001] (i.e., E-, C-, and B-type CPO, respectively) (e.g., Katayama et al., 2004; Jung et al., 2006, 2013, 2014). Insofar as the bimodal CPO reported in this study and that of Tasaka et al. (2016) (Figs. 1 and 2) results from deformation dominated by the (001)[100] and (100)[001] slip systems, it may be considered transitional between the E-type and C-type CPOs. In previous experimental studies, the transition between E-type and C-type CPOs occurred at water contents of 600–1000 ppm H/Si in samples deformed at equivalent stresses of >100 MPa (Katayama et al., 2004; Jung et al., 2006). Indeed, the water content of 1160 ppm H/Si in the experimentally deformed Fo<sub>50</sub> places it on the boundary between E-type and C-type CPO projected to lower stresses. The concentration of  $100 \pm 20$  ppm H/Si estimated for olivine in the xenolith, which is broadly typical of water contents in exhumed peridotites (Peslier, 2010; Warren and Hauri, 2014), represents a lower bound on the water content of olivine during deformation due to the possibility of subsequent water loss through processes such as re-equilibration at lower pressures or with the kimberlite melt. Therefore, it seems likely that the water content of PHN1611 at the time of deformation was just right to balance activity of the (001)[100] and (100)[001] slip systems and develop the bimodal CPO. In this case, the bimodal CPO may be common at depth in regions where water contents and CPOs span the boundary between E-type and C-type.

We note that Bernard and Behr (2017) did not observe a correlation between water contents of olivine and the occurrence of either A-type or E-type CPO in a suite of peridotite xenoliths from California. However, the general difficulty in constraining the relative timings of deformation and (de)hydration leave open possible histories in which preserved CPOs may not reflect the slip systems favoured by the recorded hydration states. Nonetheless, the role of water in promoting the (001)[100] and (100)[001] slip systems is underscored by the contrast between the bimodal CPO developed in the water-saturated experiments of Tasaka et al. (2016) and the unimodal A-type CPO developed in experiments on nominally anhydrous olivine of otherwise similar composition and experimental conditions (e.g., Hansen et al., 2012, 2014).

Changes in relative slip system activity as a function of water content require anisotropy in the mechanism by which water im-

pacts slip system activity. Single crystals of olivine deformed at high temperature under anhydrous conditions exhibit  $n = 3.5$  for all slip systems (Bai et al., 1991), consistent with climb-controlled strain rates limited by Si pipe diffusion along dislocation cores (Hirth and Kohlstedt, 2015). With the addition of water, all slip systems exhibit  $n \approx 2.5$  (Mackwell et al., 1985), consistent with climb-controlled strain rate limited by Si lattice diffusion (Tielke et al., 2017). The equality of stress exponents for different slip systems indicates that the anisotropic effects of water on slip system activity do not arise from a stress-dependent mechanism (Karato et al., 2008). Karato et al. (2008) hypothesise that such CPO transitions arise from anisotropic increases in the density of jogs, which control rates of climb, along dislocation lines under jog-undersaturated conditions (e.g., Mei and Kohlstedt, 2000). Hydration may impact dislocation self-energy, and hence jog density, in an anisotropic manner, but such effects remain poorly characterised.

#### 4.3. Impact of bimodal crystallographic preferred orientation on seismic properties

The velocities of seismic waves travelling through mantle rocks are commonly inferred to be controlled by the CPO of olivine, which constitutes the largest volume fraction of peridotites. Due to the anisotropic elastic properties of the olivine lattice, the CPO of olivine is expressed as anisotropy in seismic wave speeds of the bulk rock (Ben Ismail and Mainprice, 1998). As such, observations of seismic anisotropy can potentially constrain the kinematics of mantle flow if the relationship between CPO and flow kinematics can be inferred. However, the relationships between flow kinematics and olivine CPO can be varied and complex due to the variety of CPO types that can form, even for kinematically simple deformations (e.g., Skemer and Hansen, 2016). For the CPO types most commonly observed to develop during simple shear in the high-strain regime of approximately steady-state microstructure, the orientation of maximum P-wave speed is typically approximately parallel or perpendicular to the shear direction and/or shear plane (Jung et al., 2006). However, Fig. 8 reveals that the bimodal CPO of PHN1611 (Fig. 2) generates a maximum in P-wave velocity at approximately 45° between the inferred shear direction and shear plane normal. The microstructure of PHN1611 (e.g., laterally continuous layers of dynamically recrystallised pyroxene, Fig. 2) and comparison to olivine CPO in the experiments of Tasaka et al. (2016) suggest that PHN1611 has been deformed to shear strains of at least several hundred percent and that its CPO has likely reached its approximately steady-state configuration. The asymmetry of the xenolith microstructure (Fig. 2) and similarity of its bimodal CPO to that formed in the experiments of Tasaka et al. (2016) and VPSC simulations (Figs. 6 and 7) indicates that the natural deformation was dominantly simple shear. Comparison of the seismic properties calculated based on only olivine and those calculated based on the full major mineral assemblage indicate that the olivine CPO controls the orientation distributions of seismic wave speeds, whereas the other minerals act to reduce the speeds overall (Fig. 8). The unequal strengths of the [100] maxima result in a pronounced maximum in P-wave velocity bisecting the shear direction and shear plane normal (Fig. 8). In contrast, two maxima are present in both the velocities of the fast S-wave and in shear wave splitting (AVs), and are aligned with the shear direction and shear plane normal (Fig. 8). As the fast shear wave polarises parallel to the (010) plane of olivine single crystals (Ben Ismail and Mainprice, 1998), the strong [010] maximum in the CPO of the PHN1611 (Fig. 2) causes wave propagating in most directions to be polarised in the plane that contains the shear direction and shear plane normal (Fig. 8). These distributions of seismic properties differ those associated with previously reported unimodal

olivine CPOs (Jung et al., 2006) and therefore present an additional complication for interpreting the kinematics of mantle flow without *a priori* knowledge or prediction of the CPO type present at depth. We note that the bimodal CPO of PHN1611 is clearly scarce in natural samples (e.g., Ben Ismail and Mainprice, 1998). Nonetheless, sampling by xenolith suites of mantle deformation fabrics is necessarily limited in both space and time, and therefore the bimodal CPO remains potentially under-represented.

## 5. Conclusions

Recent torsion experiments on aggregates of hydrous olivine by Tasaka et al. (2016) were the first to reproduce an unusual and previously unexplained CPO, characterised by bimodal distributions of [100] and [001] axes, present in a lherzolite xenolith from Lesotho (Mercier and Carter, 1985). HR-EBSD analysis demonstrates that samples with the bimodal CPO contain substructure dominated by (010)[100], (001)[100], and (100)[001] edge dislocations, whereas anhydrous olivine deformed under otherwise similar conditions generally lacks (100)[001] edge dislocations. Similarly, VPSC simulations indicate that the bimodal CPO develops when deformation is dominated by the (001)[100] and (100)[001] slip systems, with a more minor contribution from (010)[100]. Olivine in the xenolith is estimated to have contained  $100 \pm 20$  ppm H/Si when last in equilibrium with clinopyroxene, providing a lower bound on the water content during deformation. The combined evidence from CPO types, GND/misorientation analyses, VPSC simulations, and water concentration measurements indicates that elevated concentrations of hydrous point defects promote relative activity of the (001)[100] and (100)[001] slip systems, leading to formation of the bimodal CPO. Unlike previously reported CPO types, the bimodal CPO generates a maximum in P-wave velocity that bisects the shear direction and shear plane normal, whereas maxima in  $V_{s1}$  and  $AV_s$  are parallel to both the shear direction and shear plane normal. If large volumes of mantle contain olivine with the bimodal CPO, then these distributions of seismic wave speeds complicate the interpretation of mantle flow kinematics from seismic anisotropy, unless the CPO type present at depth is independently constrained.

## Acknowledgements

We thank Graham Pearson and Peter Nixon for providing a sample of xenolith PHN1611 and David Mainprice for discussions its microstructure. D. Wallis, L.N. Hansen, and A.J. Wilkinson acknowledge support from the Natural Environment Research Council Grant NE/M000966/1. M. Tasaka acknowledges support through a JSPS Research Fellowship for Young Scientists (26-4879) and the Japan Society for the Promotion of Science (16K17832). D.L. Kohlstedt acknowledges support through NASA Grant NNX15AL53G. K.M. Kumamoto acknowledges support through NSF Division of Earth Science grants 1255620 and 1625032. Any opinions, findings, and conclusions or recommendations expressed in this material are those of the authors and do not necessarily reflect the views of NSF.

## Appendix A. Supplementary material

Supplementary material related to this article can be found online at <https://doi.org/10.1016/j.epsl.2018.12.007>.

## References

Allsopp, H., Bristow, J.W., Smith, C.B., Brown, R., Gleadow, A.J.W., Kramers, J.D., Garvic, O., 1989. A summary of radiometric dating methods applicable to kimberlites and related rocks. In: Ross, J.L. (Ed.), *Kimberlites and Related Rocks*.

- Their Composition, Occurrence, Origin and Emplacement*. Blackwell, Oxford, pp. 349–357.
- Aubaud, C., Withers, A.C., Hirschmann, M.M., Guan, Y., Leshin, L.A., Mackwell, S.J., Bell, D.R., 2007. Inter-calibration of FTIR and SIMS for hydrogen measurements in glasses and nominally anhydrous minerals. *Am. Mineral.* 92, 811–828. <https://doi.org/10.2138/am.2007.2248>.
- Bai, Q., Mackwell, S.J., Kohlstedt, D.L., 1991. High-temperature creep of olivine single crystals 1. Mechanical results for buffered samples. *J. Geophys. Res.* 96, 2441–2463. <https://doi.org/10.1029/90JB01723>.
- Bass, J.D., 1995. Elasticity of minerals, glasses, and melts. In: Ahrens, T.J. (Ed.), *Mineral Physics and Crystallography: a Handbook of Physical Constants*. American Geophysical Union, Washington, DC.
- Ben Ismail, W., Mainprice, D., 1998. An olivine fabric database: an overview of upper mantle fabrics and seismic anisotropy. *Tectonophysics* 296, 145–157. [https://doi.org/10.1016/S0040-1951\(98\)00141-3](https://doi.org/10.1016/S0040-1951(98)00141-3).
- Bernard, R.E., Behr, W.M., 2017. Fabric heterogeneity in the Mojave lower crust and lithospheric mantle in Southern California. *J. Geophys. Res., Solid Earth* 122, 5000–5025. <https://doi.org/10.1002/2017JB014280>.
- Britton, T.B., Wilkinson, A.J., 2011. Measurement of residual elastic strain and lattice rotations with high resolution electron backscatter diffraction. *Ultramicroscopy* 111, 1395–1404. <https://doi.org/10.1016/j.ultramic.2011.05.007>.
- Cao, Y., Jung, H., Song, S., Park, M., Jung, S., Lee, J., 2015. Plastic deformation and seismic properties in fore-arc mantles: a petrofabric analysis of the Yushigou harzburgites, north Qilian suture zone, NW China. *J. Petrol.* 56, 1897–1944. <https://doi.org/10.1093/petrology/egv053>.
- Carswell, D.A., 1991. The garnet-orthopyroxene Al barometer: problematic application to natural garnet lherzolite assemblages. *Mineral. Mag.* 55, 19–31.
- Castelnau, O., Blackman, D.K., Lebensohn, R.A., Ponte Castañeda, P., 2008. Micromechanical modeling of the viscoplastic behaviour of olivine. *J. Geophys. Res.* 113, B09202. <https://doi.org/10.1029/2007JB005444>.
- Chopra, P.N., Paterson, M.S., 1981. The experimental deformation of dunite. *Tectonophysics* 78, 453–473. [https://doi.org/10.1016/0040-1951\(81\)90024-X](https://doi.org/10.1016/0040-1951(81)90024-X).
- Darot, M., Gueguen, Y., 1981. High-temperature creep of forsterite single crystals. *J. Geophys. Res., Solid Earth* 86, 6219–6234. <https://doi.org/10.1029/JB086iB07p06219>.
- Demouchy, S., Tommasi, A., Barou, F., Mainprice, D., Cordier, P., 2012. Deformation of olivine in torsion under hydrous conditions. *Phys. Earth Planet. Inter.* 202–203, 56–70. <https://doi.org/10.1016/j.pepi.2012.05.001>.
- Hansen, L.N., Zhao, Y.-H., Zimmerman, M.E., Kohlstedt, D.L., 2014. Protracted fabric evolution in olivine: implications for the relationship among strain, crystallographic fabric, and seismic anisotropy. *Earth Planet. Sci. Lett.* 387, 157–168. <https://doi.org/10.1016/j.epsl.2013.11.009>.
- Hansen, L.N., Zimmerman, M.E., Dillman, A.M., Kohlstedt, D.L., 2012. Strain localization in olivine aggregates at high temperature: a laboratory comparison of constant-strain-rate and constant-stress boundary conditions. *Earth Planet. Sci. Lett.* 333–334, 134–145. <https://doi.org/10.1016/j.epsl.2012.04.016>.
- Hauri, E.H., Gaetani, G.A., Green, T., 2006. Partitioning of water during melting of the Earth's upper mantle at H<sub>2</sub>O-undersaturated conditions. *Earth Planet. Sci. Lett.* 248, 715–734. <https://doi.org/10.1016/j.epsl.2006.06.014>.
- Hirth, G., Kohlstedt, D.L., 2015. The stress dependence of olivine creep rate: implications for extrapolation of lab data and interpretation of recrystallised grain size. *Earth Planet. Sci. Lett.* 418, 20–26. <https://doi.org/10.1016/j.epsl.2015.02.013>.
- Jung, S., Jung, H., Austrheim, H., 2014. Characterisation of olivine fabrics and mylonite in the presence of fluid and implications for seismic anisotropy and shear localization. *Earth Planets Space* 66, 46. <https://doi.org/10.1186/1880-5981-66-46>.
- Jung, H., Karato, S.-I., 2001. Water-induced fabric transitions in olivine. *Science* 293, 1460–1463. <https://doi.org/10.1126/science.1062235>.
- Jung, H., Katayama, I., Jiang, Z., Hiraga, T., Karato, S.-I., 2006. Effect of water and stress on the lattice-preferred orientation of olivine. *Tectonophysics* 421, 1–22. <https://doi.org/10.1016/j.tecto.2006.02.011>.
- Jung, H., Lee, J., Ko, B., Jung, S., Park, M., Cao, Y., Song, S., 2013. Natural type-C olivine fabrics in garnet peridotites in North Qaidam UHP collisional belt, NW China. *Tectonophysics* 594, 91–102. <https://doi.org/10.1016/j.tecto.2013.03.025>.
- Jung, H., Mo, W., Choi, S.H., 2009. Deformation microstructures of olivine in peridotite from Spitsbergen, Svalbard, and implications for seismic anisotropy. *J. Metamorph. Geol.* 27, 707–720. <https://doi.org/10.1111/j.1525-1314.2009.00838.x>.
- Karato, S.-I., Jung, H., Katayama, I., Skemer, P., 2008. Geodynamic significance of seismic anisotropy of the upper mantle: new insights from laboratory studies. *Annu. Rev. Earth Planet. Sci.* 36, 59–95. <https://doi.org/10.1146/annurev.earth.36.031207.124120>.
- Karato, S.-I., Paterson, M.S., Fitzgerald, J.D., 1986. Rheology of synthetic olivine aggregates—influence of grain size and water. *J. Geophys. Res.* 91, 8151–8176. <https://doi.org/10.1029/JB091iB08p08151>.
- Katayama, I., Jung, H., Karato, S.-I., 2004. New type of olivine fabric from deformation experiments at modest water content and low stress. *Geology* 32, 1045–1048. <https://doi.org/10.1130/G20805>.
- Kerschhofer, L., Sharp, T.G., Rubie, D.C., 1996. Intracrystalline transformation of olivine to wadsleyite and ringwoodite under subduction zone conditions. *Science* 274, 79–81. <https://doi.org/10.1126/science.274.5284.79>.



- Koga, K.T., Hauri, E.H., Hirschmann, M.M., Bell, D.R., 2003. Hydrogen concentration analyses using SIMS and FTIR: comparison and calibration for nominally anhydrous minerals. *Geochim. Geophys. Geosyst.* 4, 1–20. <https://doi.org/10.1029/2002GC000378>.
- Kohlstedt, D.L., Ricoult, D.L., 1984. High-temperature creep of silicate olivines. In: Tressler, R.E., Bradt, R.C. (Eds.), *Deformation of Ceramic Materials II*. Springer, US, pp. 251–280.
- Kumamoto, K.M., Warren, J.M., Hauri, E.H., 2017. New SIMS reference materials for measuring water in upper mantle minerals. *Am. Mineral.* 102, 537–547. <https://doi.org/10.2138/am-2017-5863CCBYNCND>.
- Lebensohn, R.A., Tomé, C.N., 1993. A self-consistent anisotropic approach for the simulation of plastic deformation and texture development of polycrystals: application to zirconium alloys. *Acta Metall. Mater.* 41, 2611–2624. [https://doi.org/10.1016/0956-7151\(93\)90130-K](https://doi.org/10.1016/0956-7151(93)90130-K).
- Liu, Y., Ponte Castañeda, P., 2004. Second-order theory for the effective behaviour and field fluctuations in viscoplastic polycrystals. *J. Mech. Phys. Solids* 52, 467–495. [https://doi.org/10.1016/S0022-5096\(03\)00078-4](https://doi.org/10.1016/S0022-5096(03)00078-4).
- Mackwell, S.J., Kohlstedt, D.L., Paterson, M.S., 1985. The role of water in the deformation of olivine single crystals. *J. Geophys. Res.* 90, 11319–11333. <https://doi.org/10.1029/JB090iB13p11319>.
- Mainprice, D., Hielscher, R., Schaeben, H., 2011. Calculating anisotropic physical properties from texture data using the MTEX open-source package. *Geol. Soc. (Lond.) Spec. Publ.* 360, 175–192. <https://doi.org/10.1144/SP360.10>.
- Mei, S., Kohlstedt, D.L., 2000. Influence of water on plastic deformation of olivine aggregates: 1. Dislocation creep regime. *J. Geophys. Res.* 105, 21471–21481. <https://doi.org/10.1029/2000JB900180>.
- Mercier, J.-C., Carter, N.L., 1985. Pyroxene geotherms. *J. Geophys. Res.* 80, 3349–3362. <https://doi.org/10.1029/JB080i023p03349>.
- Mizukami, T., Wallis, S.R., Yamamoto, J., 2004. Natural examples of olivine lattice preferred orientation patterns with a flow-normal  $a$ -axis maximum. *Nature* 427, 432–436. <https://doi.org/10.1038/nature02179>.
- Nixon, P.H., Boyd, F.R., 1973. Petrogenesis of the granular and sheared ultrabasic nodule suite in kimberlites. In: Nixon, P.H. (Ed.), *Lesotho Kimberlites*. Cape and Transvaal Printers, pp. 48–56.
- Nye, J.F., 1953. Some geometrical relations in dislocated crystals. *Acta Metall.* 1, 153–162. [https://doi.org/10.1016/0001-6160\(53\)90054-6](https://doi.org/10.1016/0001-6160(53)90054-6).
- O'Leary, J.A., Gaetani, G.A., Hauri, E.H., 2010. The effect of tetrahedral Al<sup>3+</sup> on the partitioning of water between clinopyroxenes and silicate melt. *Earth Planet. Sci. Lett.* 297, 111–120. <https://doi.org/10.1016/j.epsl.2010.06.011>.
- Paterson, M.S., 1982. The determination of hydroxyl by infrared absorption in quartz, silicate glasses and similar materials. *Bull. Mineral.* 105, 20–29.
- Pearson, D.G., Carlson, R.W., Shirby, S.B., Boyd, F.R., Nixon, P.H., 1995. Stabilisation of Archean lithospheric mantle: a Re–Os isotope study of peridotite xenoliths from the Kaapvaal craton. *Earth Planet. Sci. Lett.* 134, 341–357. [https://doi.org/10.1016/0012-821X\(95\)00125-V](https://doi.org/10.1016/0012-821X(95)00125-V).
- Peslier, A.H., 2010. A review of water contents of nominally anhydrous natural minerals in the mantles of Earth, Mars and the Moon. *J. Volcanol. Geotherm. Res.* 197, 239–258. <https://doi.org/10.1016/j.jvolgeores.2009.10.006>.
- Prior, D.J., 1999. Problems in determining the misorientation axes, for small misorientations, using electron backscatter diffraction in the SEM. *J. Microsc.* 195, 217–225. <https://doi.org/10.1046/j.1365-2818.1999.00572.x>.
- Raleigh, C.B., 1968. Mechanisms of plastic deformation of olivine. *J. Geophys. Res.* 73, 5391–5406. <https://doi.org/10.1029/JB073i016p05391>.
- Raterron, P., Girard, J., Chen, J., 2012. Activities of olivine slip systems in the upper mantle. *Phys. Earth Planet. Inter.* 200–201, 105–112. <https://doi.org/10.1016/j.pepi.2012.04.006>.
- Skemer, P., Hansen, L.N., 2016. Inferring upper-mantle flow from seismic anisotropy: an experimental perspective. *Tectonophysics* 668–669, 1–14. <https://doi.org/10.1016/j.tecto.2015.12.003>.
- Skemer, P., Katayama, I., Karato, S.-I., 2006. Deformation fabrics of the Cima di Gagnone peridotite massif, Central Alps, Switzerland: evidence of deformation at low temperatures in the presence of water. *Contrib. Mineral. Petrol.* 152, 43–51. <https://doi.org/10.1007/s00410-006-0093-4>.
- Tasaka, M., Zimmerman, M.E., Kohlstedt, D.L., 2015. Creep behaviour of Fe-bearing olivine under hydrous conditions. *J. Geophys. Res., Solid Earth* 120, 6039–6057. <https://doi.org/10.1002/2015JB012096>.
- Tasaka, M., Zimmerman, M.E., Kohlstedt, D.L., 2016. Evolution of the rheological and microstructural properties of olivine aggregates during dislocation creep under hydrous conditions. *J. Geophys. Res., Solid Earth* 121, 92–113. <https://doi.org/10.1002/2015JB012134>.
- Tenner, T.J., Hirschmann, M.M., Withers, A.C., Hervig, R.L., 2009. Hydrogen partitioning between nominally anhydrous upper mantle minerals and melt between 3 and 5 GPa and applications to hydrous peridotite partial melting. *Chem. Geol.* 262, 42–56. <https://doi.org/10.1016/j.chemgeo.2008.12.006>.
- Tharimena, S., Rychert, C., Harmon, N., 2017. A unified continental thickness from seismology and diamonds suggests a melt-defined plate. *Science* 357, 580–583. <https://doi.org/10.1126/science.aan0741>.
- Tielke, J.A., Zimmerman, M.E., Kohlstedt, D.L., 2017. Hydrolytic weakening in olivine single crystals. *J. Geophys. Res., Solid Earth* 122, 3465–3479. <https://doi.org/10.1002/2017JB014004>.
- Tommasi, A., Mainprice, D., Canova, G., Chastel, Y., 2000. Viscoplastic self-consistent and equilibrium-based modeling of olivine lattice preferred orientations: implications for the upper mantle seismic anisotropy. *J. Geophys. Res.* 105, 7893–7908. <https://doi.org/10.1029/1999JB900411>.
- Wallis, D., Hansen, L.N., Britton, T.B., Wilkinson, A.J., 2016. Geometrically necessary dislocation densities in olivine obtained using high-angular resolution electron backscatter diffraction. *Ultramicroscopy* 168, 34–45. <https://doi.org/10.1016/j.ultramicro.2016.06.002>.
- Wallis, D., Hansen, L.N., Britton, T.B., Wilkinson, A.J., 2017a. Dislocation interactions in olivine revealed by HR-EBSD. *J. Geophys. Res., Solid Earth* 122, 7659–7678. <https://doi.org/10.1002/2017JB014513>.
- Wallis, D., Parsons, A.J., Hansen, L.N., 2017b. Quantifying geometrically necessary dislocations in quartz using HR-EBSD: application to chessboard subgrain boundaries. *J. Struct. Geol.* <https://doi.org/10.1016/j.jsg.2017.12.012>.
- Warren, J.M., Hauri, E.H., 2014. Pyroxenes as tracers of mantle water variations. *J. Geophys. Res.* 119, 1851–1881. <https://doi.org/10.1002/2013JB010328>.
- Wilkinson, A.J., 2001. A new method for determining small misorientations from electron back scatter diffraction patterns. *Scr. Mater.* 44, 2379–2385. [https://doi.org/10.1016/S1359-6462\(01\)00943-5](https://doi.org/10.1016/S1359-6462(01)00943-5).
- Wilkinson, A.J., Meaden, G., Dingley, D., 2006. High resolution mapping of strains and rotations using electron backscatter diffraction. *Mater. Sci. Technol.* 22, 1271–1278. <https://doi.org/10.1179/174328406X130966>.
- Wilkinson, A.J., Randman, D., 2010. Determination of elastic strain fields and geometrically necessary dislocation distributions near nanoindentations using electron back scatter diffraction. *Philos. Mag.* 90, 1159–1177. <https://doi.org/10.1080/14786430903304145>.
- Withers, A.C., Hirschmann, M.M., Tenner, T.J., 2011. The effect of Fe on olivine H<sub>2</sub>O storage capacity: consequences for H<sub>2</sub>O in the martian mantle. *Am. Mineral.* 96, 1039–1053. <https://doi.org/10.2138/am.2011.3669>.
- Zhang, S., Karato, S.-I., 1995. Lattice preferred orientation of olivine aggregates deformed in simple shear. *Nature* 375, 774–777. <https://doi.org/10.1038/375774a0>.
- Zhang, S., Karato, S.-I., Gerald, J.F., Faul, U.H., Zhou, Y., 2000. Simple shear deformation of olivine aggregates. *Tectonophysics* 316, 133–152. [https://doi.org/10.1016/S0040-1951\(99\)00229-2](https://doi.org/10.1016/S0040-1951(99)00229-2).
- Zhao, Y.H., Ginsberg, S.B., Kohlstedt, D.L., 2004. Solubility of hydrogen in olivine: dependence on temperature and iron content. *Contrib. Mineral. Petrol.* 147, 155–161. <https://doi.org/10.1007/s00410-003-0524-4>.
- Zhong, X., Frehner, M., Kunze, K., Zappone, A., 2014. A novel EBSD-based finite-element wave propagation model for investigating seismic anisotropy: application to Finero Peridotite, Ivrea-Verbano Zone, Northern Italy. *Geophys. Res. Lett.* 41, 7105–7114. <https://doi.org/10.1002/2014GL060490>.